Superelasticity of slim hysteresis over a wide temperature range by nanodomains of martensite

Dong Wang [a,b], Sen Hou [a], Yu Wang [a], Xiangdong Ding [a], Shuai Ren [a], Xiaobing Ren [a,c], Yunzhi Wang [a,d,*]

[a] *Center of Microstructure Science, Multi-Disciplinary Materials Research Center, Frontier Institute of Science and Technology, State Key Laboratory for Mechanical Behavior of Materials, Xi'an Jiaotong University, Xi'an 710049, China*
[b] *State Key Laboratory for Strength and Vibration of Mechanical Structures, Xi'an Jiaotong University, Xi'an 710049, China*
[c] *Ferroic Physics Group, National Institute for Materials Science, Tsukuba, 305-0047 Ibaraki, Japan*
[d] *Department of Materials Science and Engineering, The Ohio State University, 2041 College Road, Columbus, OH 43210, USA*

Abstract

By nanostrain-domain engineering of shape memory alloys (SMAs) via impurity doping, we show a new mechanism that leads to superelasticity with slim hysteresis across a wide temperature range. Three-dimensional computer simulations using the Landau theory of phase transformations and Khachaturyan's microelasticity theory predict the formation of randomly distributed nanosized, single-variant martensitic domains in Fe-doped NiTi SMAs. These nanoscale martensitic domains are frustrated and cannot evolve into long-range-ordered, internally twinned structures (i.e. long-range strain ordering). Such a structural state is found to evolve gradually upon loading and unloading or heating and cooling across a wide temperature range with narrow hysteresis. The simulation predictions have been confirmed by experiments carried out by doping a conventional SMA, $Ti_{50}Ni_{48}Fe_2$, with extra Fe into a new composition of $Ti_{50}Ni_{44}Fe_6$.
© 2013 Acta Materialia Inc. Published by Elsevier Ltd. All rights reserved.

Keywords: Phase field simulation; Martensitic nanodomains; Stress–strain curve; Martensitic transformation; Strain glass transition

1. Introduction

The unique properties of shape memory alloys (SMAs), such as shape memory effect (SME) and superelasticity (SE), originate from structural phase transformations with symmetry breaking that produce self-accommodating poly-twin domain structures [1–5]. Sensing and actuation can be realized through domain switching under external fields. Even though these microdomain structures and related applications in various materials systems have been studied for over a century [3–10], the properties of their nanodomain counterpart have not yet been explored until

recently [11–17]. We show in this study that randomly distributed nanodomains of individual martensitic variants does offer a remarkable superelasticity not seen in common SMAs – superelasticity of slim hysteresis over a wide temperature range. Large hysteresis and narrow temperature range of superelasticity associated with the conventional microdomain structures have been limiting the usefulness of SMAs in devices that require high sensitivity, high precision, high durability and high energy efficiency in complex environments. For example, large hysteresis may result in inaccurate position feedback of robotic actuators [5] and produce undesirable fatigue damage and low durability of cardiovascular stents [18,19]. Thus the present work could shed light on the development of new SMAs of much improved performance for advanced applications through nanostrain-domain engineering.

---

* Corresponding author at: Department of Materials Science and Engineering, The Ohio State University, 2041 College Road, Columbus, OH 43210, USA.

E-mail address: wang.363@osu.edu (Y. Wang).

It has been shown that reducing the grain size of austenite down to below 50 nm can decrease significantly the width of the hysteresis loop [20,21]. However, preparing SMAs with grain sizes below 50 nm is still a difficult challenge, even with the applications of modern material processing techniques. Most recently, a simulation study [22,23] reported that with the vanishing of structural anisotropy of a low-symmetry precipitate phase, stress hysteresis decreases rapidly and giant non-hysteretic strain response could be achieved by stress-induced direct switching of nanoprecipitates from one orientation variant to another. However, any shape changes of the nanoprecipitates are confined by the surrounding matrix phase where they are embedded. Since the matrix phase is non-transforming, plastic deformation in the matrix phase may have to be considered in order to accommodate the shape changes of the precipitates. In addition, crystallographic compatibility has been used as a criterion to search for SMAs of low hysteresis, but the criterion can be satisfied only in limited SMAs until now (i.e. the Ti–Ni–Cu–Pd system) [18,24]. Simultaneously, the narrow temperature regions of superelasticity limit the application of SMAs in complex environments, such as high-integrity seals, joints and controls of a broad variety in the automobile, aeroplane and space industries. Omori et al. have tried to enlarge the superlasticity temperature regions through developing new SMAs by decreasing the temperature dependence of cricial stress (i.e. the Clausius–Clapeyron relation) [25], but this method is not suitable for well-studied SMAs (e.g. TiNi).

Here we propose a method to reduce the stress–strain hysteresis and to enlarge the temperature range of SE by nano-straindomain engineering in conventional SMAs. The basic idea is to use local lattice distortion created by point defects or other extended defects such as dislocations and misfitting clusters or nanoprecipitates to prevent autocatalytic events and the sudden formation of long-range ordered, internally twinned structure (i.e. long-range strain ordering), and "freeze" gradually the SMAs into a strain state of randomly distributed, nanosized, single-variant martensitic domains. Domain switching and confined domain growth are anticipated to be the major events during loading and unloading and thus slim hysteresis is expected because of the lack of nucleation and twinning/detwinning events. We first use computer simulations to show that impurity doping does create effectively such a microstructural state and such a microstructural state does offer superelasticity with slim hysteresis over a wide temperature range. We then confirm experimentally that extra impurity doping of a conventional SMA changes the large hysteresis into a slim one and widens significantly the temperature range of superelasticity.

2. Model

Both theoretical and experimental studies have shown that impurity doping reduces martensitic domain size

[11–15,26–29]. In our present model system, the point defects considered are Fe atoms replacing Ni atoms at the Ni sublattice in B2 NiTi austenite [28], which create local lattice distortion due to either atomic size difference or chemical effects [30,31]. The roles played by these point defects in the martensitic transformation are described in the model by introducing two effects [14,26,32,33], a local field effect (LFE) and a global transition temperature effect (GTTE). Computer simulations have shown that it is the LFE associated with randomly distributed point defects that generates frustrated martensitic nanodomains that cannot develop into long-range ordered, internally twinned structure (i.e. long-range strain ordering) [14]. The GTTE alters the thermodynamic stability of martensite (i.e. changes the martensitic transition temperature of the system). Based on the framework of the Landau theory of phase transformations with symmetry reduction [2,34], gradient thermodynamics [35], microelasticity theory [36], and with the incorporation of the above-mentioned two effects from point defects [14], three-dimensional (3-D) phase field simulations for a cubic phase → trigonal phase (R phase) martensitic transformation in an Fe-doped TiNi system are carried out [37].

2.1. Cubic to trigoinal phase transformation in TiNi-based SMAs

The cubic (B2) → trigonal (R) martensitic phase transformation takes place along four crystallographically equivalent and hence energetically degenerate Bain paths and generates four deformation variants, which are described by four non-conserved order parameters, $\eta_1(\mathbf{r})$, $\eta_2(\mathbf{r})$, $\eta_3(\mathbf{r})$ and $\eta_4(\mathbf{r})$, in the Landau free energy. Any given microstructural state in the system can be described by local values of these four order parameters, e.g. $(\eta_1, \eta_2, \eta_3, \eta_4) = (0, 0, 0, 0)$ represents the austenite and $(\eta_1, \eta_2, \eta_3, \eta_4) = (1, 0, 0, 0)$, $(0, 1, 0, 0), (0, 0, 1, 0)$ or $(0, 0, 0, 1)$ represnets one of the four deformation variants of the R phase, respectively.

The stress-free transformation strain (SFTS) of the $B2 \rightarrow R$ transformation can be calculated according to the lattice parameters of the R phase $a_R = 0.73388$ nm and $c_R = 0.52838$ nm [38], and that of the B2 phase $a_{B2} = 0.3015$ nm [39], and the lattice correspondence between the B2 and R phases [4], as shown in Table 1. Accordingly, in the reference coordinate N1, i.e. $x//[1\,0\,0]_R$, $y//[0\,1\,0]_R$, $z//[0\,0\,1]_R$ in the basis of the R phase, the transformation matrix that describes a homogenous lattice deformation from B2 to R [39] is:

$$\varepsilon_{N1}^R = \begin{pmatrix} \frac{a_R - \sqrt{6}a_{B2}}{\sqrt{6}a_{B2}} & 0 & 0 \\ 0 & \frac{a_R - \sqrt{6}a_{B2}}{\sqrt{6}a_{B2}} & 0 \\ 0 & 0 & \frac{c_R - \sqrt{3}a_{B2}}{\sqrt{3}a_{B2}} \end{pmatrix} = \begin{pmatrix} -0.006284 & 0 & 0 \\ 0 & -0.006284 & 0 \\ 0 & 0 & 0.0118 \end{pmatrix}$$

In the reference coordinate N2, i.e. $x//[1\,0\,0]_{B2}$, $y//[0\,1\,0]_{B2}$, $z//[0\,0\,1]_{B2}$ in the basis of the B2 phase, the SFTSs of the four variants can be calculated by

$\varepsilon^R(i) = T(i)\varepsilon^R_{N1}T(i)^{-1}$, where $i = 1, 2, 3, 4$ and $\mathrm{T}(i)$ is the rotation matrix mapping between N1 and N2 coordinates for the four variants:

$$T(1) = \begin{pmatrix} \frac{1}{\sqrt{6}} & \frac{1}{\sqrt{6}} & \frac{1}{\sqrt{3}} \\ \frac{-2}{\sqrt{6}} & \frac{1}{\sqrt{6}} & \frac{1}{\sqrt{3}} \\ \frac{1}{\sqrt{6}} & \frac{-2}{\sqrt{6}} & \frac{1}{\sqrt{3}} \end{pmatrix}, \quad T(2) = \begin{pmatrix} \frac{-1}{\sqrt{6}} & \frac{1}{\sqrt{6}} & \frac{1}{\sqrt{3}} \\ \frac{2}{\sqrt{6}} & \frac{1}{\sqrt{6}} & \frac{1}{\sqrt{3}} \\ \frac{1}{\sqrt{6}} & \frac{2}{\sqrt{6}} & \frac{-1}{\sqrt{3}} \end{pmatrix},$$

$$T(3) = \begin{pmatrix} \frac{2}{\sqrt{6}} & \frac{1}{\sqrt{6}} & \frac{1}{\sqrt{3}} \\ \frac{1}{\sqrt{6}} & \frac{-1}{\sqrt{6}} & \frac{-1}{\sqrt{3}} \\ \frac{-1}{\sqrt{6}} & \frac{-2}{\sqrt{6}} & \frac{1}{\sqrt{3}} \end{pmatrix}, \quad T(4) = \begin{pmatrix} \frac{2}{\sqrt{6}} & \frac{-1}{\sqrt{6}} & \frac{-1}{\sqrt{3}} \\ \frac{1}{\sqrt{6}} & \frac{1}{\sqrt{6}} & \frac{1}{\sqrt{3}} \\ \frac{1}{\sqrt{6}} & \frac{-2}{\sqrt{6}} & \frac{1}{\sqrt{3}} \end{pmatrix},$$

and the results are:

$$\varepsilon^R(1) = \begin{pmatrix} -0.000246 & 0.006038 & 0.006038 \\ 0.006038 & -0.000246 & 0.006038 \\ 0.006038 & 0.006038 & -0.000246 \end{pmatrix},$$

$$\varepsilon^R(2) = \begin{pmatrix} -0.000246 & 0.006038 & -0.006038 \\ 0.006038 & -0.000246 & -0.006038 \\ -0.006038 & -0.006038 & -0.000246 \end{pmatrix}$$

$$\varepsilon^R(3) = \begin{pmatrix} -0.000246 & -0.006038 & 0.006038 \\ -0.006038 & -0.000246 & -0.006038 \\ 0.006038 & -0.006038 & -0.000246 \end{pmatrix}$$

$$\varepsilon^R(4) = \begin{pmatrix} -0.000246 & -0.006038 & -0.006038 \\ -0.006038 & -0.000246 & 0.006038 \\ -0.006038 & 0.006038 & -0.000246 \end{pmatrix}$$

2.2. Energetics

The total free energy, F,

$$F = \int d^3\mathbf{r}[f_{ch}(\eta_1, \cdots \eta_4) + f_L + f_{gr}(\eta_1, \cdots \eta_4)] + E_{el}$$
$$+ E_{applied} \tag{1}$$

of the system consists of the following contributions.

(a) local chemical free energy is approximated by a Landau polynomial:

$$f_{ch}(\eta_1, \cdots \eta_4) = \frac{1}{2}A_1 \sum_{i=1,\cdots 4} \eta_i^2(\mathbf{r}) - \frac{1}{4}A_2 \sum_{i=1,\cdots 4} \eta_i^4(\mathbf{r})$$
$$+ \frac{1}{6}A_3 \left(\sum_{i=1,\cdots 4} \eta_i^2(\mathbf{r}) \right)^3 \tag{2}$$

where η_i are the structural order (SO) parameters that characterize the four symmetry-related R phase variants,

Table 1
Lattice correspondence between B2 and R phases.

Variant	$[1\,0\,0]_R$	$[0\,1\,0]_R$	$[0\,0\,1]_R$	$(0\,0\,0\,1)_R$
1	$[1\,\bar{2}\,1]_{B2}$	$[1\,1\,\bar{2}]_{B2}$	$[1\,1\,1]_{B2}$	$(1\,1\,1)_{B2}$
2	$[\bar{1}\,2\,1]_{B2}$	$[1\,1\,2]_{B2}$	$[1\,1\,\bar{1}]_{B2}$	$(1\,1\,\bar{1})_{B2}$
3	$[2\,1\,\bar{1}]_{B2}$	$[1\,\bar{1}\,2]_{B2}$	$[1\,\bar{1}\,1]_{B2}$	$(1\,\bar{1}\,1)_{B2}$
4	$[2\,1\,1]_{B2}$	$[\bar{1}\,1\,2]_{B2}$	$[\bar{1}\,1\,1]_{B2}$	$(\bar{1}\,1\,1)_{B2}$

$A_1 = A_1^0 \cdot (T - T^0(c))$, and A_1^0, A_2, A_3 and A_4 are positive constants; c is a dimensionless average defect concentration, $T^0(c) = T^{00} + b \cdot c$ ($T^{00} = 300$ K, $b = -300$ and $c = 0.03$ for $\mathrm{Ti}_{50}\mathrm{Ni}_{44}\mathrm{Fe}_6$ in our simulations); and b characterizes the relative strength of the global transition temperature effect (GTTE). In our simulations, the real defect concentration n can be calculated through $n = c\frac{a^3 \mathrm{N}}{l_0^3 N_0}$, where c is the dimensionless concentration, a is the lattice constant, l_0 is the length scale of our simulation, N_0 is the number of total unit cells in one grid site and N is the number of defect-carrying unit cells in one grid site, and in the extreme condition, we choose $N = N_0$ in our simulations.

(b) excess energy associated with local lattice distortions $\varepsilon_{kl}^{local}(\mathbf{r})$ generated by the point defects (i.e. the LFE) is approximated by:

$$f_L(r) = C_{ijkl} \sum_{i,j,k,l=1,2,3} \varepsilon_{kl}^{local}(\mathbf{r}) \cdot \varepsilon_{ij}^R(\mathbf{r}) \tag{3}$$

In this work we assume that an Fe atom replacing Ni will create a local dilational strain of ~ 0.06 $\left(\text{i.e. } \frac{a_{bcc}^{Fe} - a_{bcc}^{Ni}}{a_{bcc}^{Ni}} \right)$. dilational strain is used to calculate the excess energy. The strain caused by MT can be described in terms of the order parameter fields and stress-free transformation strain (SFTS), i.e. $\varepsilon_{ij} = \sum_{p=1}^{4} \varepsilon_{ij}^R(p)\eta_p^2$.

(c) non-local gradient energy associated with spatial non–uniformity of the SO parameters, η_i:

$$f_{gr}(\eta_1, \cdots, \eta_4) = \frac{1}{2}\beta \left(\sum_{i=1,\cdots 4} (\nabla \eta_i)^2 \right) \tag{4}$$

where β is the gradient energy coefficient.

(d) coherency elastic strain energy associated with lattice mismatch between austenite and martensite and among different variants of the martensitic phase is formulated based on Khachaturyan's microelasticity theory [36]:

$$E_{el} = \frac{1}{2}C_{ijkl}\sum_{p=1}^{4}\sum_{q=1}^{4}\varepsilon_{ij}^R(p)\varepsilon_{kl}^R(q)\int \eta_p^2(\mathbf{r})\eta_q^2(\mathbf{r})d^3r$$
$$- \frac{1}{2}\sum_{p=1}^{4}\sum_{q=1}^{4}\int \frac{d^3k}{(2\pi)^3}B_{pq}\left(\frac{\vec{k}}{k}\right)\{\eta_p^2(\mathbf{r})\}_k\{\eta_q^2(\mathbf{r})\}_k^* \tag{5}$$

where C_{ijkl} is the elastic modulus tensor, $\mathbf{k}$ is the wave vector defined in the reciprocal space, $\{\eta_p^2(\mathbf{r})\}_k$ is the Fourier transform of $\eta_p^2(\mathbf{r})$, $\{\eta_p^2(\mathbf{r})\}_k^*$ is the complex conjugate of $\{\eta_p^2(\mathbf{r})\}_k$ and the kernel $B_{pq}(\vec{k}/k)$ is $B_{pq}(\vec{e}) = e_i\sigma_{ij}^0(p)\Omega(\vec{e})_{jk}\sigma_{kl}^0(q)e_l$, where $\vec{e} = \vec{k}/k$, $\sigma_{ij}^0(p) = c_{ijkl}\varepsilon_{ij}^R(p)$, $\Omega(\vec{e})_{ij}^{-1} = c_{ijkl}e_ke_l$.

(e) elastic energy caused by external load is given by:

$$E_{applied} = -\sigma \cdot \bar{\varepsilon} = -\int \sigma_{ij} \cdot \sum_{i=1,\cdots 4} \varepsilon^R(i)\eta_i^2(r)d^3r \tag{6}$$

where σ is the external load, and $\bar{\varepsilon}$ is the average strain. In the simulations, a sinusoidal external stress $\sigma = \sigma_0 \sin(2\pi\omega t)$ is

applied, with $\sigma_0 = 600$ MPa and $\omega = \frac{1}{N\Delta t}$ (where N is the number of dimensionless time steps and Δt is the real time unit of one dimensionless time step). For $N = 5 \times 10^5$ used in the simulations, we have $N\Delta t = 5.7 \times 10^{-6}$ s and $\omega = 1.75 \times 10^5$ Hz.

The real material parameters used in the simulations are: elastic constants of the parent phase $C_{11} = 200$ GPa, $C_{12} = 150$ GPa and $C_{44} = 50$ GPa (homogeneous modulus assumption, i.e. the austenite and martensite having the same elastic modulus, is made), the driving force [40] for the austenite to R martensite transformation $\Delta f_{A \rightarrow M} = -1.86 \times 10^6$ J/m³, the coherent interfacial energy between two martensitic variants $\gamma_{MM} = 0.05$ J/m² and the interfacial energy between austenite and martensite can be predicted as $\gamma_{AM} = \gamma_{MM}/2$ (ratio $\frac{\gamma_{MM}}{\gamma_{AM}} \approx 2$ is obtained from the simulations).

The dimensionless parameters (with superscript*) used in our simulations are chosen according to the relationship between physical and dimensionless parameters [41]: elastic strain energy $E_{el}^* = \frac{E_{el}}{\Delta f_{scale}}$ and elastic constants $C_{ij}^* = \frac{C_{ij}}{\Delta f_{scale}}$, chemical free energy $f_{ch}^* = \frac{f_{ch}}{\Delta f_{scale}}$ and chemical free energy coefficients $A_i^* = \frac{A_i}{\Delta f_{scale}}$, gradient energy $\gamma_{gr}^* = \frac{\gamma_{gr}}{\Delta f_{scale} l_0}$ and gradient energy coefficient $\beta^* = \frac{\beta}{\Delta f_{scale} l_0^2}$, excess free energy $f_L^* = \frac{f_L}{\Delta f_{scale}}$, temperature $T^* = \frac{T}{T^{00}}$, noise term $\zeta^* = \frac{\zeta}{\Delta f_{scale} M_\eta}$, length scale $r^* = \frac{r}{l_0}$ and time scale $t^* = \frac{t M_\eta \Delta f_{scale}}{M^*}$ (t is the real time). The energy scaling factor to reduce each physical parameter into a dimensionless quantity is chosen as $\Delta f_{scale} = 10^7$ J/m³ and the length scale of our simulation cell (i.e. grid size) is $l_0 = 1$ nm according to the interfacial energy $\gamma_{MM} = 0.05$ J/m².

Thus the free energy can be written in the following dimensionless form:

$$F^* = \int d^3\mathbf{r}^* [f_{ch}^*(\eta_1, \cdots \eta_4) + f_L^* + f_{gr}^*(\eta_1, \cdots \eta_4)] + E_{el}^* + E_{applied}^*. \tag{7}$$

The following values of the dimensionless parameters are used in our simulations: $A_1^{0*}=20$ (and $A_1^* = A_1^{0*} \cdot (T^* - T^{0*}(c))$), $A_2^*=32.05$, $A_3^*=37.5$, $\beta^* = 1.5$ and the elastic constants $C_{11}^* = 2 \times 10^4$, $C_{12}^* = 1.5 \times 10^4$, $C_{44}^* = 5 \times 10^3$. The system size considered in the simulations is 64 nm × 64 nm × 64 nm with a 64 × 64 × 64 numerical mesh and periodical boundary conditions are applied along all three dimensions.

2.3. Kinetics

The stochastic time-dependent Ginsburg–Landau equation is used for the time-evolution of the SO parameters:

$$\frac{\partial \eta_p(\mathbf{r}, t)}{\partial t^*} = -M^* \frac{\delta F^*}{\delta \eta_p(\mathbf{r}, t)} + \zeta_p^*(\mathbf{r}, t), \quad p = 1, 2, 3, 4 \tag{8}$$

where ζ^* is the dimensionless noise term describing thermal fluctuations, F^* is the dimensionless total free energy of the

system, η is the structural order (SO) parameters, t^* is the dimensionless time, M^* is the kinetic coefficient and $M^* = 1.0$ in reduced unit is used in the simulations.

Since the martensitic transformation (MT) in NiTi alloys occurs at a speed approaching the velocity of sound wave propagating in solids, we assume that the interface between martensite and austenite moves during the transformation at a velocity of $\sim10^3$ m/s in our model system. Based on the relationship between velocity and driving force $v = M(-\Delta f)$ [42], and considering the typical driving force $\Delta f = 1.86 \times 10^6$ J/m³ for B2 $\rightarrow$ R transformation in the TiNiFe system [40], the physical interface mobility can be calculated as $M = 5.3 \times 10^{-4}$ m⁴ J⁻¹ s⁻¹. Then following the relationship [42] between the physical interface mobility and the phase field mobility that describes the time evolution of the order parameter fields in the phase field equation, M_η, we have $M_\eta = M \int_\delta (\frac{d\eta}{dx})^2 dx = M \frac{\gamma_{AM}}{\beta} = 8.8 \times 10^5$ m³ J⁻¹ s⁻¹, where δ (the integration limit) is the interface width in phase field simulations, $\gamma_{AM} = 0.025$ J/m² and $\beta = \Delta f_{scale} \beta^* l_0^2 = 1.5 \times 10^{-11}$ J/m. Then the time step in physical units can be calculated as $\Delta t = \frac{\Delta t^* M^*}{M_\eta \Delta f_{scale}} = 1.14 \times 10^{-11}$ s, where Δt^* and M^* (the dimensionless time step and mobility) are set to 1 in our simulations.

The Langevin force term in the phase field method is assumed to be uncorrelated in both space and time, and the first and second moments satisfy [41]:

$$\langle \varsigma_p(\mathbf{r}, t) \rangle = 0 \tag{9}$$

$$\langle \varsigma_p(\mathbf{r}, t) \varsigma_p(\mathbf{r}', t') \rangle = 2 k_B T M_\eta \delta(t - t') \delta(\mathbf{r} - \mathbf{r}'). \tag{10}$$

In discrete forms, these conditions become

$$\langle \varsigma_p(n, m) \rangle = 0 \tag{11}$$

$$\langle \varsigma_p(n, m) \varsigma_p(n', m') \rangle = 2 k_B T M_\eta \frac{\delta_{mm'}}{\Delta t} \frac{\delta_{nn'}}{l_0^d} \tag{12}$$

where n and m are respectively the indices of discrete spatial position and time, Δt is the time step, l_0 is the grid size, d is the dimensionality of the space and δ_{ij} is the Kronecker delta. Then the Langevin force terms can be emulated with a random number generator ρ_i, with Gaussian distribution, and satisfy $\langle \rho_i \rangle = 0$ and $\langle \rho_i \rho_{i'} \rangle = \delta_{ii'}$, i.e. $\zeta_p(n, m) = \sqrt{2 k_B T M_\eta / (l_0^3 \Delta t)} \rho$ [41], and the dimensionless Langevin force term can be described as $\zeta^* = \frac{\zeta}{\Delta f_{scale} M_\eta} \approx 0.08 \rho$ in our simulations at 300 K.

3. Results

3.1. Hysteresis under thermal cycling at different defect concentrations

The simulation results obtained upon cooling from austenite at defect concentrations $n = 0$ at.% (i.e. Ni$_{50}$Ti$_{50}$) and $n = 6$ at.% (i.e. Ti$_{50}$Ni$_{44}$Fe$_6$) are shown in Fig. 1. The red, blue, green and yellow colors represent the four martensitic

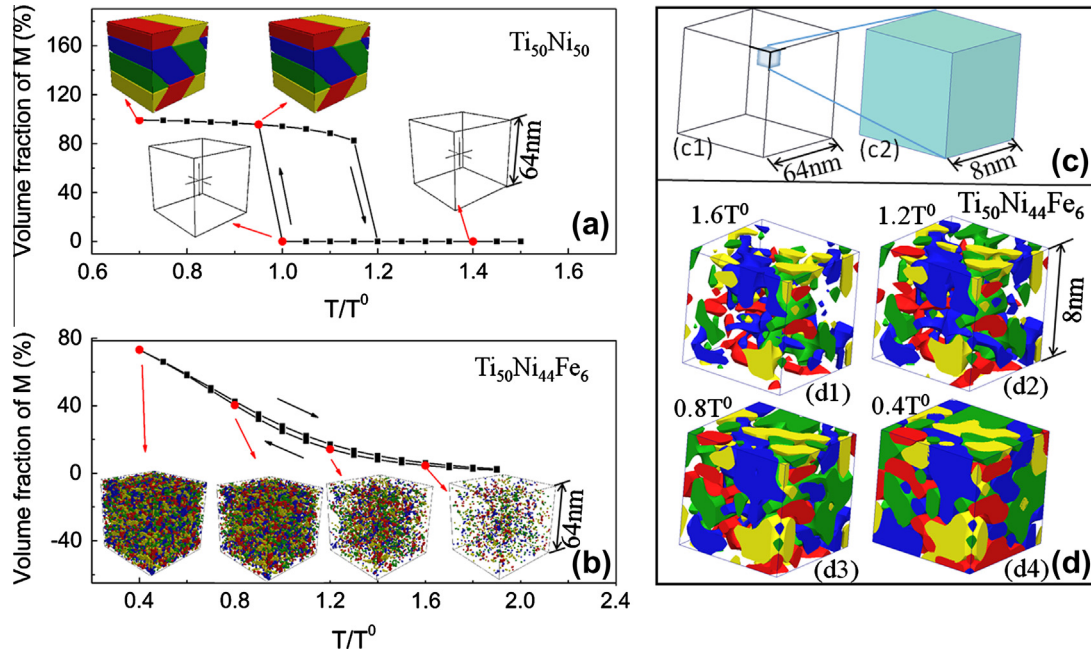Fig. 1. Microstructural evolutions and volume fraction changes during a cubic → trigonal (R phase) normal martensitic transformation in $Ti_{50}Ni_{50}$ (a) and strain glass transition in $Ti_{50}Ni_{44}Fe_6$ (b) obtained by phase field simulations in three dimensions. The black arrows indicate the cooling and heating processes, respectively. (c) Schematics of zooming into the microstructure. (d) Portions of enlarged images (as indicated in (c)) of the microstructures shown in (b). In the micrographs, red, blue, yellow and green represent the four variants of the R martensite. (For interpretation of the references to colour in this figure legend, the reader is referred to the web version of this article.)

variants. In the case of $Ni_{50}Ti_{50}$ (see Fig. 1a), the system transforms upon cooling into regular R martensite with a typical self-accommodating, long-range ordered, internally twinned structure (i.e. long-range strain ordering). The martensitic volume fraction shows a sudden change at T^0 upon cooling (where T^0 is the martensitic transformation start temperature, and is used to normalize the temperature) and a large hysteresis between cooling and heating.

In contrast, randomly distributed martensitic nanodomains are developed in the case of $Ti_{50}Ni_{44}Fe_6$ (see Fig. 1b). The martensitic volume fraction changes are almost reversible upon cooling and heating, leading to a narrow hysteresis. Nanodomains of single variant of

martensite start to appear at temperatures far above T^0, indicating that randomly distributed point defects stabilize locally certain martensitic variants. However, these nanodomains cannot grow into long-range ordered, internally twinned structure (i.e. long-range strain ordering) as normally seen in martensitic crystals (Fig. 1a) because they are randomly distributed in space. This is similar to the incompatible ground states found in magnetic systems [43] where competing interactions prevent the formation of an ordered ground state because the long-range interactions in all three ferroic systems are parallel to each other in nature. In a confined ferroelastic system, the long-range elastic interactions prefer the formation of a martensitic
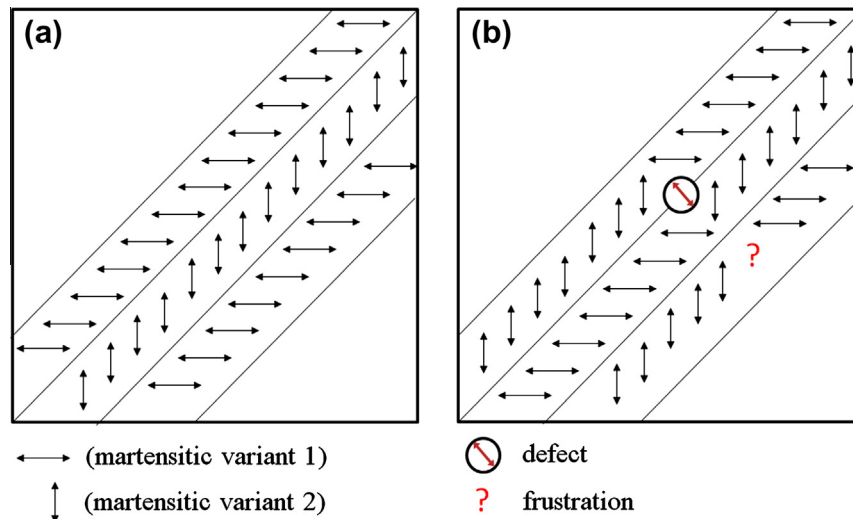

Fig. 2. Schematic illustration of (a) normal martensitic ground state (perfect twin) without defects and (b) strain frustration caused by a point defect.
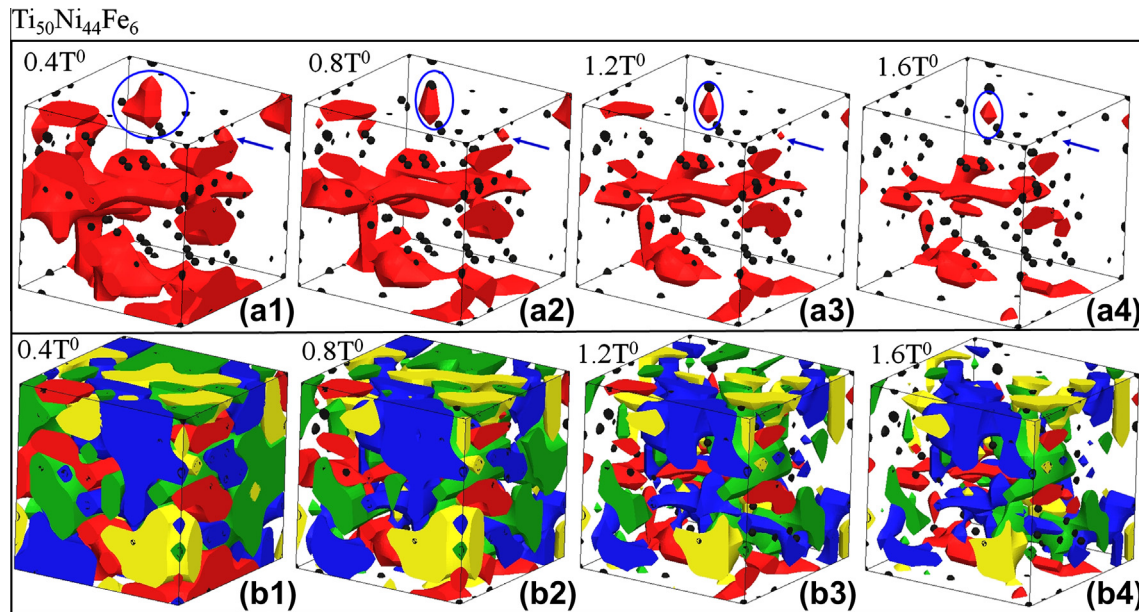
Fig. 3. Microstructural evolutions during strain glass transition in $Ti_{50}Ni_{44}Fe_6$. (a1)–(a4) Microstructural evolutions of martensitic variant 1 upon cooling; blue arrows point to the nucleation event under cooling and blue circles describe the growth event under cooling. (b1)–(b4) Microstructural evolutions of all martensitic variants upon cooling. Black represents the defects, red, blue, yellow and green represent the four variants of the R martensite. (For interpretation of the references to colour in this figure legend, the reader is referred to the web version of this article.)

ground state, i.e. a self-accommodated internally twinned morphological pattern, as shown schematically in Fig. 2a, which has the minimum elastic strain energy. However, when random defects exist, local strain/stress fields (also infinitely long-range in nature) associated with these random defects interfere (i.e. interact) with the transformation strain and prevent the formation of such a ground state (as shown schematically in Fig. 2b). As a consequence, a strain glass state consisting of randomly distributed nanodomains of individual martensitic variants is formed instead.

To show the detailed evolution of the nanodomain structures in $Ti_{50}Ni_{44}Fe_6$, we zoom into the initial microstructures of $Ti_{50}Ni_{44}Fe_6$ according to Fig. 1c and show the enlarged images in Fig. 1d. From Fig. 1d and Fig. 3 we can see clearly the gradual increase of irregular shaped martensitic nanodomains in the system upon cooling, but the final domain size is limited by the spacing among the random point defects. Figs. 3a1–a4 shows the detailed evolutions of domain structures with only martensitic variant 1 (red) and defects (black), from which we can see that the domiant event upon cooling is the growth of existing domains, as indicated by the blue circles, with limited nulceeation events (indicated by the blue arrows). Figs. 3b1–b4 shows the domain structure evolutions with all martensitic variants (red, blue, green and yellow) and defects (black).

3.2. Superelasticity of SMAs at different defect concentrations

The calculated stress–strain curves for $Ti_{50}Ni_{50}$ and $Ti_{50}Ni_{44}Fe_6$ at different temperatures are shown in Figs. 4a and b, respectively. A tensile stress along the [1 1 1] direction is applied, which prefers martensitic variant 1 (red). In the

case of $Ti_{50}Ni_{50}$ (Fig. 4a), the system shows clearly superelasticity at high temperatures. The stress-induced austenite (A) $\rightarrow$ martensite (M) transformation and the reverse M $\rightarrow$ A transformation occur at two nearly constant stress levels, leading to a wide stress plateau and a large hysteresis loop. At low temperatures, superelasticity vanishes and large remnant strain appears because of the difficulty of new domain nucleation. There exists a detwinning process (multi-domains $\rightarrow$ single domain) because of domain wall motions under loading. Because the stable phase at low temperatures is the martensitic phase, the single domain after loading cannot go back and results in large remnant strain under unloading. In the case of $Ti_{50}Ni_{44}Fe_6$ (see Fig. 4b), the stress–strain curves show superelasticity with narrow hysteresis and nearly zero remnant strain across a wide temperature range and there is no stress plateau in the stress–strain curves.

To validate the simulation predictions, we carry out experimental studies of the effect of doping on stress–strain hysteresis in TiNiFe systems. Previous experimental observations [28,29] have reported the existence of martensitic nanodomains in this system. All samples are solution-treated at 1273 K for 1 h followed by water quenching. A Shimadzu AG-IS tensile machine and a Kyowa strain gage are used to measure the stress and strain. Fig. 4c shows the stress–strain curves of $Ti_{50}Ni_{48}Fe_2$, a normal SMA, at different temperatures. We find that the system shows SE at high temperatures and SME at low temperatures but with large hysteresis. When extra Fe is doped into the system to a new alloy composition of $Ti_{50}Ni_{44}Fe_6$ (Fig. 4d), superelastic behavior is observed across a wide temperature range and the hysteresis of the stress–strain curves becomes much narrower, with much smaller remnant strain after
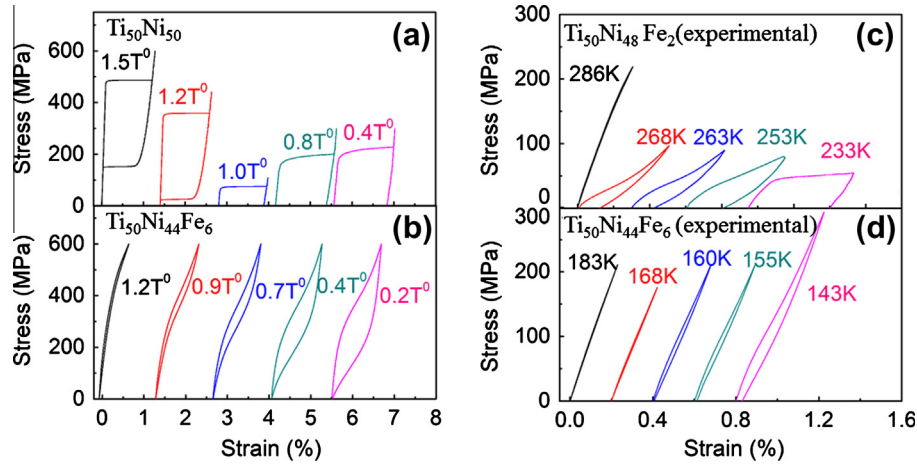
Fig. 4. Calculated stress–strain curves for (a) $Ti_{50}Ni_{50}$ and (b) $Ti_{50}Ni_{44}Fe_6$ at different temperatures and experimentally measured stress–strain curves for (c) $Ti_{50}Ni_{48}Fe_2$ (a normal martensitic composition) and (d) $Ti_{50}Ni_{44}Fe_6$ (a strain glass composition) at different temperatures.

unloading. Our calculated stress–strain curves (Figs. 4a and b) seem to agree well with the experimentally measured ones (Figs. 4c and d). However, note that the small hysteresis (without stress plateau) at high temperature shown in Fig. 4c is not predicted by our simulations shown in Fig. 4a. This could be attributed to the fact that the SFTS of R in TiNi is temperature-dependent. It was shown that the SFTS of the R phase in TiNi-based shape memory alloys decreases sharply with increasing temperature [44]. At high temperatures, the SFTS of R is so small that it results in an almost linear response in the stress–strain curve with small hysteresis and no obvious plateau. When temperature is lowered, the SFTS of R increases and the system begins to show normal hysteresis with a plateau. Our experimental results agree well with those reported previously [44]. In the simulations, however, we have assumed that the SFTS of the R phase has a relative large value (1%) and is temperature-independent. This assumption could have resulted in the difference between the simulation prediction and experiment observations.

Besides the $TiNi_{50-x}Fe_x$ alloys considered in the current study, recent experimental studies of $Ni_{55-x}Co_xFe_{18}Ga$ [45] and $TiNbO_x$ [46] alloys also show similar results, i.e. the hysteresis loops change from sharp with plateau to smooth and slim with increasing defect concentrations. We believe that the change of the stress–strain curves in these experiments could be caused by the same mechanism as those we have demonstrated in the simulations, i.e. martensitic nanodomains caused by the doped defects.

4. Discussion

In order to understand the drastically different hysteretic behaviors of the two systems ($Ti_{50}Ni_{50}$, $Ti_{50}Ni_{44}Fe_6$), we show in Figs. 5 and 6 the microstructural evolutions corresponding to different points on the stress–strain curves. Fig. 5a and b shows the stress–strain curves and the corresponding microstructures for the case of $Ti_{50}Ni_{50}$ at temperatures $1.5T^0$ and $0.8T^0$, respectively. The insets describe the related microstructural evolution. Fig. 5a show
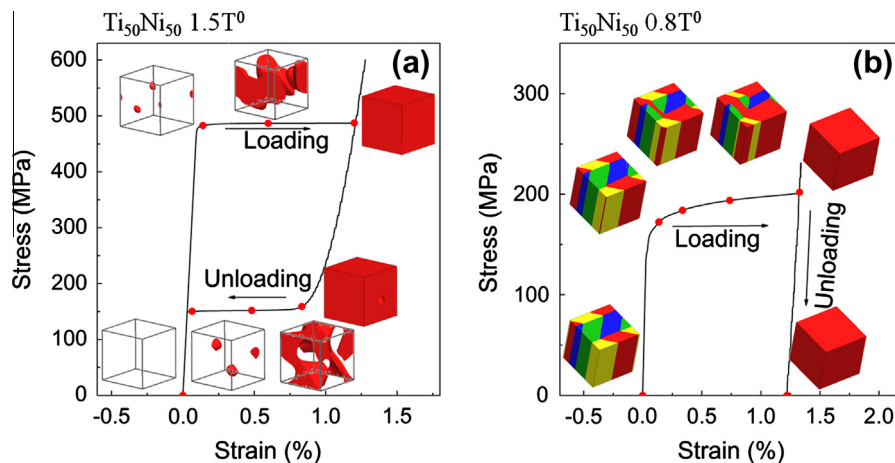

Fig. 5. Calculated stress–strain curves and corresponding microstructural evolutions for $Ti_{50}Ni_{50}$ at (a) $T = 1.5T^0$ and (b) $T = 0.8T^0$. The parent phase is transparent and the four martensitic variants are red, green, blue and yellow. (For interpretation of the references to colour in this figure legend, the reader is referred to the web version of this article.)
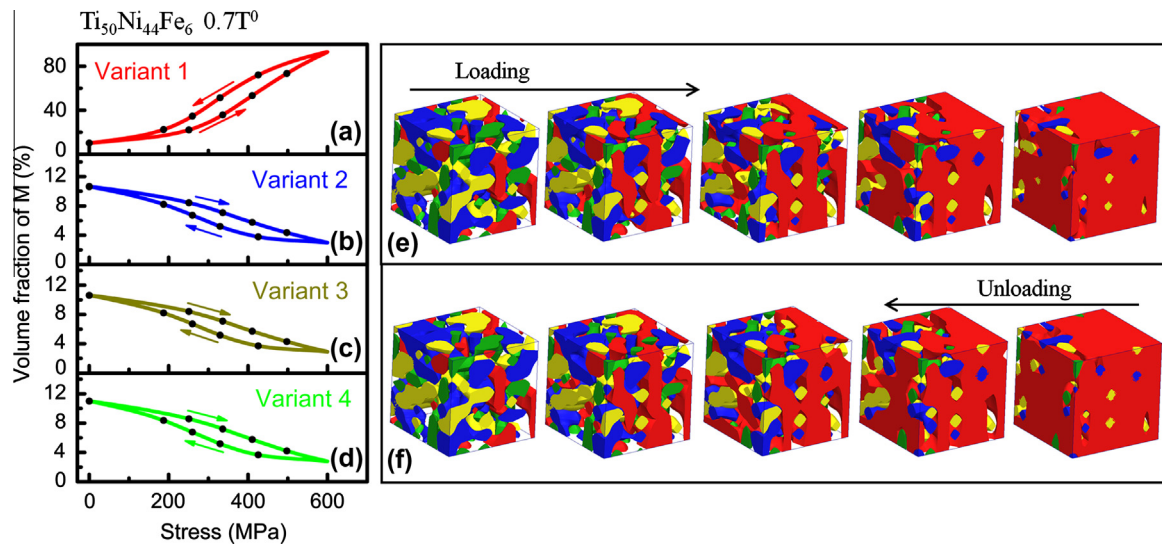
Fig. 6. (a−d) Calculated volume fraction changes of the four martensitic variants in $Ti_{50}Ni_{44}Fe_6$ under loading and unloading processes (as indicated by arrows). (e and f) The corresponding microstructural evolution (to the black dots in (a)) in a portion of the system with four martensitic variants represented by red, blue, yellow and green, respectively. (For interpretation of the references to colour in this figure legend, the reader is referred to the web version of this article.)
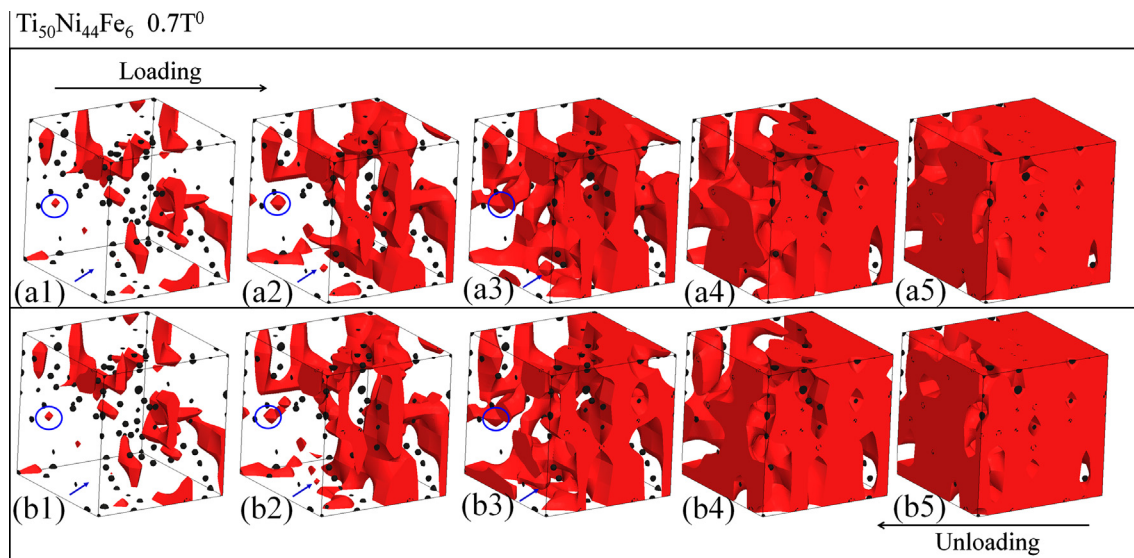

Fig. 7. Microstructural evolutions of martensitic variant 1 under loading (a) and unloading (b) of strain glass transition in $Ti_{50}Ni_{44}Fe_6$ at $T = 0.7T^0$. (a1)–(a5) Loading process, blue arrows point to the nucleation event under loading and blue circles describe the growth event under loading. (b1)–(b5) Unloading process. In the micrographs, black represents the defects; red represents the martensitic variant 1. (For interpretation of the references to colour in this figure legend, the reader is referred to the web version of this article.)

superelasticity with a large hysteresis at $T = 1.5T^0$ where the stable phase is austenite (transparent). A critical applied load is needed to induce the nucleation of martensite. The large hysteresis is associated with the large difference between the critical stress for nucleation of martensite (variant 1) under loading and the critical stress for nucleation of austenite under unloading (see the inset microstructures). Fig. 5b shows detwinning with large remnant strain at $T = 0.8T^0$, where the stable phase is martensite with four variants arranged in a poly-twin structure. The applied stress prefers martensitic variant 1 (red) and induces a single domain state through domain wall motion. Upon unloading, the difficulty of nucleating other

variants in such a single-variant state results in large remnant strain and hysteresis. The critical stress for detwinning in our simulation is from the Peierls stress caused by domain wall motion [47].

Figs. 6a–d show respectively the volume fraction changes of different martensitic variants as a function of stress at $T = 0.7T^0$ obtained for $Ti_{50}Ni_{44}Fe_6$. It is readily seen that variant 1 (Fig. 6a), which is preferred by the applied load, shows a gradual increase (decrease) in volume fraction upon loading (unloading), while the other three variants (Figs. 6b–d) show the opposite. The microstructures corresponding to the black dots in Fig. 6a during loading and unloading are shown in Figs. 6e and f, respectively.
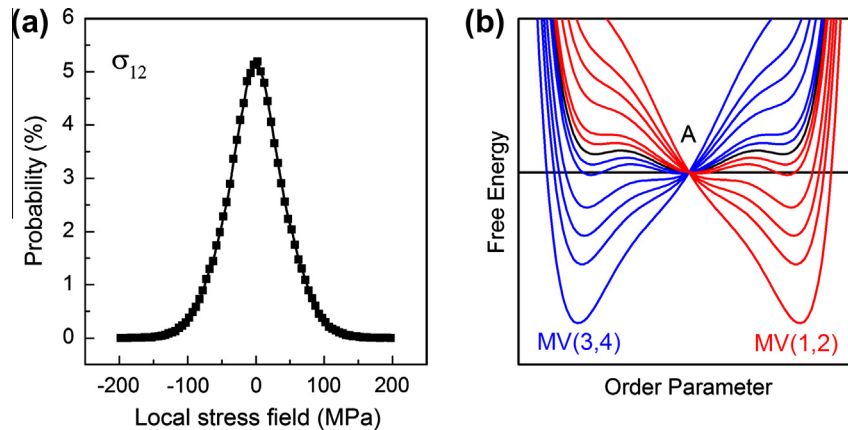
Fig. 8. (a) Local stress field (σ_{12}) distribution caused by defects in our model system (Ti$_{50}$Ni$_{44}$Fe$_{6}$). The stress fields are calculated through the linear superposition of the local stress fields caused by a single defect. (b) Schematic drawings of free energy landscapes showing the effect of local local stress field in (a). The "MV(1,2)", "MV(3,4)" and "A" represent martensitic variants 1 and 2, martensitic variants 3 and 4, and austenite, respectively.

Upon loading, the systems transform gradually from a state consisting of nanodomains of all four variants having approximately equal volume fractions into nanodomains consisting dominantly of variant 1 (red) that is favored by the load, but with retained nanodomains of the other variants that are favored by the local fields associated with the point defects. Upon unloading, these local fields tend to restore gradually the original multi-variants state without the need for nucleating new martensitic domains because the embryos of these domains already exist. As a direct consequence, there is no plateau in the stress–strain curves and the strain increases gradually when the stress increases. This is in contrast to the detwinning process of normal twinned martensitic plates shown in Fig. 5b, where the volume fraction of the favored variant keeps increasing at a stress level above the critical stress required for detwinning until the system reaches a uniform single domain state, leading to a plateau on the stress–strain curve. This is also in sharp contrast to the stress-strain behavior shown in Fig. 5a, where nucleation of martensite in austenite (high T) or new variants in a single martensitic domain (low T) becomes difficult and causes large hysteresis. Figs. 7a and b show the detailed microstructural evolutions of martensitic variant 1 with defects. There exist limited nucleation (blue arrows) and growth (blue circles) events under loading, which results in a gradual volume increase of martensitic variant 1. The system is difficult to reach the single domain state after loading because of the existence of LFE caused by randomly distributed defects. Under unloading, the domains of martensitic variant 1 decrease gradually and the system restores to its original state easily.

Fig. 8a shows the local stress field distribution probability of our model system Ti$_{50}$Ni$_{44}$Fe$_{6}$. Although single point defects show dilation strain and related stress distribution, the linear superposition of the stress fields of all defects produce this continuous local stress field distribution. Fig. 8b shows the related free energy plots with different local stress field. This superposition of the local stress fields from the randomly distributed point defects creates a

"potency" (activation energy barrier for nucleation by tempeature or external stress) distribution of sites at which martensitic nanodomains are formed. At a given temperature/external stress, the most potent sites (with the lowest activation energy barrier) are activated first. This local stress field distribution caused by point defects is the physical origin of continuous transformation characteristics and slim hysteresis of strain glass system.

Note that our results are obtained by the application of a sinusoidal external stress and thus the hysteresis may depend on the frequency of the external stress. The calculated stress–strain curves of normal MT and strain glass systems with changing frequencies of the applied sinusoidal stress field are shown in Fig. 9. All frequencies are normalized by $\omega_0 = 1.75 \times 10^5$ Hz (the frequency used in obtaining the results given in Fig. 4). Fig. 9a shows the superelastic behavior of the normal MT system Ti$_{50}$Ni$_{50}$ and Fig. 9b shows the superelastic behavior of a strain glass system Ti$_{50}$Ni$_{50}$Fe$_{6}$. Below the frequency $\sim 50\omega_0$, as one can readily see from Fig. 9a, the critical stress and hysteresis of superelasticity decrease with decreasing frequency, but the hysteresis is large in the entire frequency range considered. Fig. 9b shows a similar characteristic frequency dependence but with much smaller hysteresis in the frequency range ($\omega < 100\omega_0$). Fig. 9c shows the frequency dependence of the hysteresis loss (integration of the stress–strain curve) for the two systems. It shows that the frequency dependence of the hysteresis loss becomes weaker and weaker with decreasing frequency for both systems at the low frequency range, and the strain glass system (Ti$_{50}$Ni$_{50}$Fe$_{6}$) exhibits a much lower hysteresis loss than that of the normal martensitic system (Ti$_{50}$Ni$_{50}$), e.g., $F_{\text{loss}}^{\text{Ti}_{50}\text{Ni}_{44}\text{Fe}_{6}} \approx 0.18 F_{\text{loss}}^{\text{Ti}_{50}\text{Ni}_{50}}$ at $\omega = \omega_0$. When the frequency is below ω_0 ($\sim 10^5$ Hz), the hysteresis loss almost reaches a constant (not zero). In addition, the hysteresis of SE in SMAs is caused mainly by (a) nucleation of martensitic variants favored by the external load, (b) domain wall
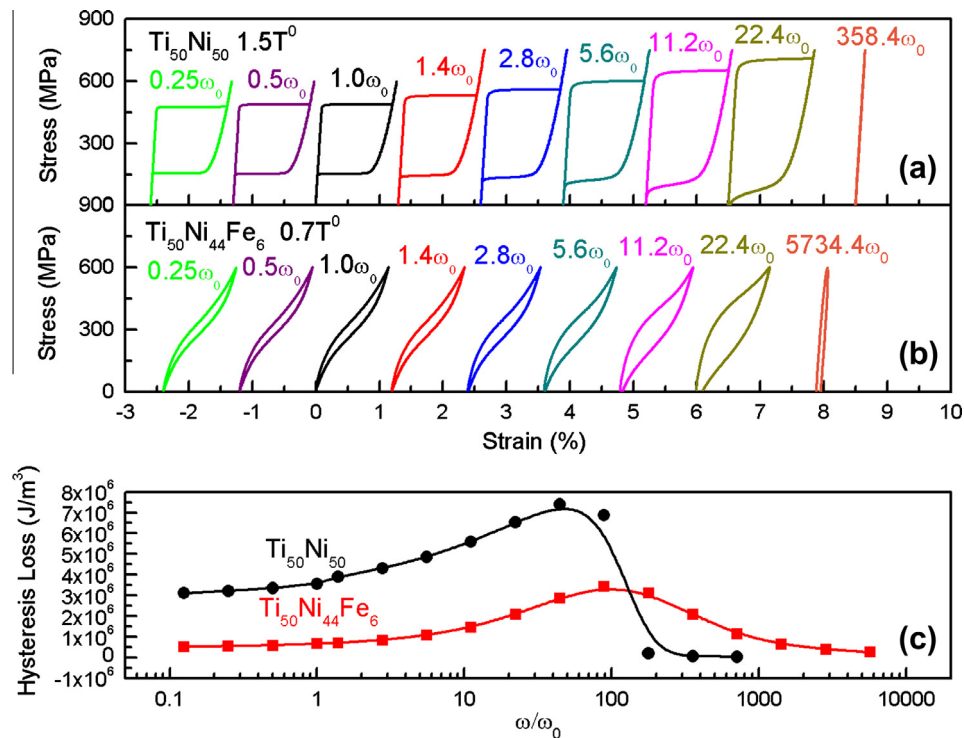
Fig. 9. Calculated stress–strain curves for (a) $Ti_{50}Ni_{50}$, at $1.5T^0$, (b) $Ti_{50}Ni_{44}Fe_6$, at $0.7T^0$, with a different frequency of external stress field. (c) Frequency dependence of hysteresis loss for $Ti_{50}Ni_{50}$ at $1.5T^0$ and $Ti_{50}Ni_{44}Fe_6$ at $0.7T^0$.

motion including detwinning (i.e. twin boundary migration) and (c) direct domain switching. The hysteresis will go to zero at the high frequency, i.e. when the frequency of the cyclic load is so high that none of the above phenomena would have enough time to take place. Calculated hysteresis at high frequency range in Fig. 9c confirms the analysis. Furthermore, the strain glass system also exhibits a much more continuous change of hysteresis (depends on frequency) than that of normal martensitic system.

5. Conclusion

We have demonstrated by both computer simulations and direct experimental measurements a method of developing unique superelastic property with slim hysteresis across a wide temperature range by nanostrain-domain engineering of shape memory alloys via impurity doping. The computer simulations reveal that the random local fields created by point defects and their superpositions stabilize nanodomains of martensite at temperatures far above the normal martensitic transformation start temperature T^0 and thus broaden significantly the temperature range of MT and hence SE. Simultaneously, the random local fields of significantly different strengths prevent the formation of a single-domain state upon loading and provide extra restoring force upon unloading. As a consequence, the reverse transformation overall does not involve nucleation events – the primary source of hysteresis. Finally, the randomness of the point defects in space suppress long-range correlation and auto-catalytic events during MT and prevent the development of long-range-

ordered, internally twinned structure (i.e. long-range strain ordering). Because of all of the above, the point defects change the normal first-order sharp martensitic transformation into a high-order like "diffuse" transition over a broad temperature range with small hysteresis.

In addition to point defects considered in the current study, any other stress-carrying defects such as dislocations and coherent precipitates [48] may also create random local fields that stabilize frustrated martensitic nanodomain structures. Thus the present work could shed light on searching SMAs with superelasticity and narrow hysteresis over a wide temperature range through defects engineering.

References

[1] Otsuka K, Wayman CM. Shape memory materials. Cambridge: Cambridge University Press; 1998.
[2] Salje EKH. Phase transitions in ferroelastic and coelastic materials. Cambridge: Cambridge University Press; 1990.

[3] Bhattacharya K. Microstructure of martensite: why it forms and how it gives rise to the shape-memory effect. Oxford: Oxford University Press; 2003.

[4] Otsuka K, Ren X. Prog Mater Sci 2005;50:511.

[5] Van Humbeeck J. Adv Eng Mater 2001;3:837.

[6] Bhattacharya K, James RD. Science 2005;307:53.

[7] Yahia H. Shape Memory Implants. Berlin: Springer; 2000.

[8] Juan JMS, No ML. Adv Mater 2008;20:272.

[9] Kohl M. Shape memory microactuators. Berlin: Springer; 2004.

[10] Duerig TW. MRS Bull 2002;27:101.

[11] Vasseur R, Lookman T. Phys Rev B 2010;81:094107.

[12] Lloveras P, Castan T, Porta M, Planes A, Saxena A. Phys Rev Lett 2008;100:165707.

[13] Sarkar S, Ren XB, Otsuka K. Phys Rev Lett 2005;95:4.

[14] Wang D, Wang Y, Zhang Z, Ren X. Phys Rev Lett 2010;105:205702.

[15] Wang Y, Ren X, Otsuka K. Phys Rev Lett 2006;97:225703.

[16] Wang Y, Song XP, Ding XD, Yang S, Zhang J, Ren XB, et al. Appl Phys Lett 2011;99:3.

[17] Zhou YM, Xue DZ, Ding XD, Otsuka K, Sun J, Ren XB. Appl Phys Lett 2009;95:3.

[18] Cui J, Chu YS, Famodu OO, Furuya Y, Hattrick-Simpers J, James RD, et al. Nat Mater 2006;5:286.

[19] Petrini Lorenza, Migliavacca F. J Metall 2011;2011:1.

[20] Cho GB, Kim VH, Hur SG, Yu CA, Nam TH. Met Mater Int 2006;12:181.

[21] Sun QP, He YJ. Int J Solids Struct 2008;45:3868.

[22] Rao WF, Khachaturyan AG. Acta Mater 2011;59:4494.

[23] Rao WF, Wuttig M, Khachaturyan AG. Phys Rev Lett 2011;106:105703.

[24] Zarnetta R, Takahashi R, Young ML, Savan A, Furuya Y, Thienhaus S, et al. Adv Funct Mater 2010;20:1917.

[25] Omori T, Ando K, Okano M, Xu X, Tanaka Y, Ohnuma I, et al. Science 2011;333:68.

[26] Semenovskaya S, Khachaturyan AG. Acta Mater 1997;45:4367.

[27] Sherrington D. J Phys Condens Matter 2008;20:304213.

[28] Wang D, Zhang Z, Zhang JA, Zhou YM, Wang Y, Ding XD, et al. Acta Mater 2010;58:6206.

[29] Zhang J, Wang Y, Ding XD, Zhang Z, Zhou YM, Ren X, et al. Phys Rev B 2011;83:174204.

[30] Korbel S, Elsasser C. Phys Rev B 2011;84.

[31] Papanikolaou N, Zeller R, Dederichs PH, Stefanou N. Phys Rev B 1997;55:4157.

[32] Levanyuk AP, Sigov AS. Defects and structural phase transitions. New York: Gordon & Breach; 1988.

[33] Wang D, Ke XQ, Wang YZ, Gao JH, Wang Y, Zhang LX, et al. Phys Rev B 2012;86:054120.

[34] Landau LD, Lifshitz EM. Statistical Physics. 3rd ed. London: Butterworth-Heinemann; 1980.

[35] Cahn JW, Hilliard JE. J Chem Phys 1958;28(2):258.

[36] Khachaturyan AG. Theory of structural transformation in solids. New York: Wiley; 1983.

[37] Wang YZ, Li J. Acta Mater 2010;58:1212.

[38] Khalil-Allafi J, Schmahl WW, Wagner M, Sitepu H, Toebbens DM, Eggeler G. Mater Sci Eng A – Struct Mater Properties Microstruct Process 2004;378:161.

[39] Zhou N, Shen C, Wagner MFX, Eggeler G, Mills MJ, Wang Y. Acta Mater 2010;58:6685.

[40] Khalil-Allafi J, Schmahl WW, Reinecke T. Smart Mater Struct 2005;14:S192.

[41] Shen C, Simmons JP, Wang Y. Acta Mater 2007;55:1457.

[42] Huang CJ, Browne DJ, McFadden S. Acta Mater 2006;54:11.

[43] Goremychkin EA, Osborn R, Rainford BD, Macaluso RT, Adroja DT, Koza M. Nat Phys 2008;4:766.

[44] Miyazaki S, Kimura S, Otsuka K. Philos Magaz A – Phys Conden Matter Struct Defects Mech Properties 1988;57:467.

[45] Wang DP, Chen X, Nie ZH, Li N, Wang ZL, Ren Y. Wang YD. Europhys Lett 2012;98:46004.

[46] Nii Y, Arima T, Kim HY, Miyazaki S. Phys Rev B 2010;82:214104.

[47] Lee WT, Salje EKH, Goncalves-Ferreira L, Daraktchiev M, Bismayer U. Phys Rev B 2006;73:214110.

[48] Ji Y, Ding X, Lookman T, Otsuka K, Ren X. Phys Rev B 2013;87:104110.